Majorana bound states in topological insulators without a vortex

Henry F. Legg ⓘ, Daniel Loss ⓘ, and Jelena Klinovaja ⓘ
Department of Physics, University of Basel, Klingelbergstrasse 82, CH-4056 Basel, Switzerland

We consider a three-dimensional topological insulator (TI) wire with a nonuniform chemical potential induced by gating across the cross section. This inhomogeneity in chemical potential lifts the degeneracy between two one-dimensional surface state subbands. A magnetic field applied along the wire, due to orbital effects, breaks time-reversal symmetry and lifts the Kramers degeneracy at zero momentum. If placed in proximity to an *s*-wave superconductor, the system can be brought into a topological phase at relatively weak magnetic fields. Majorana bound states (MBSs), localized at the ends of the TI wire, emerge and are present for an exceptionally large region of parameter space in realistic systems. Unlike in previous proposals, these MBSs occur without the requirement of a vortex in the superconducting pairing potential, which represents a significant simplification for experiments. Our results open a pathway to the realization of MBSs in present-day TI wire devices.

I. INTRODUCTION

The non-Abelian statistics of Majorana bound states (MBSs) makes them a promising basis for fault tolerant quantum computation [1–3]. Such MBSs were originally predicted to appear at the cores of vortices in spinless topological $p_x + ip_y$ superconductors [4–6]. Fu and Kane [7] proposed that a topological superconducting phase with MBSs localized at the centers of superconducting vortices could also be present at the surface of a three-dimensional topological insulator (TI) in proximity to an *s*-wave superconductor [8].

In a related setup, MBSs have been predicted in thin TI wires that are subjected to a magnetic field parallel to the wire and where the phase of the pairing potential of the proximity-induced superconductivity winds around the wire in the form of a vortex [9]. While still in their infancy, TI wire devices have recently seen significant experimental progress [10–17]. For instance, the growth of very thin (diameter ≈ 20 nm) bulk insulating $(Bi_{1-x}Sb_x)_2Te_3$ wires with quantum confined surface states was reported in Ref. [16].

Experimentally, the requirement of a vortex in the induced pairing potential essentially necessitates a full superconducting shell, which is a significant fabrication challenge. For the thinnest wires, where the effects coming from the TI bulk states are weakest, this also requires strong magnetic fields ≈ 6 T. When the superconductor is attached to only one side of the wire, such that a vortex is not expected, the superconducting gap in the topological phase was shown to be negligibly small [18–20], meaning that MBSs have very long localization lengths and will overlap in realistic finite-length wires. Hence, the prerequisite for a vortex presents a major roadblock to the realization of MBSs in current TI wire devices.

In this work, we propose an alternative protocol for obtaining MBSs in TI wires without the requirement of a superconducting vortex. This is accomplished by a metallic gate placed below the wire and a superconductor attached to the top (as shown in Fig. 1). Such a setup is very natural since

gating will almost always be required to tune the system to the Dirac point [16]. The nonuniform chemical potential induced by a finite gate voltage breaks inversion symmetry, splitting the doubly degenerate one-dimensional (1D) subbands of the quantum confined TI surface states. A magnetic field applied parallel to the wire opens a gap at momentum $k = 0$ due to orbital effects and leaves only a pair of (almost) helical modes at finite Fermi momenta. As a result, when, in addition, the superconductivity in the TI wire is induced by proximity to an *s*-wave bulk superconductor, a topological superconducting phase can be achieved. In contrast with a TI wire in which inversion symmetry is not broken by gating, this topological phase, induced without the requirement of a vortex, is characterized by a relatively large superconducting gap in the spectrum. As a consequence, the topological phase with well
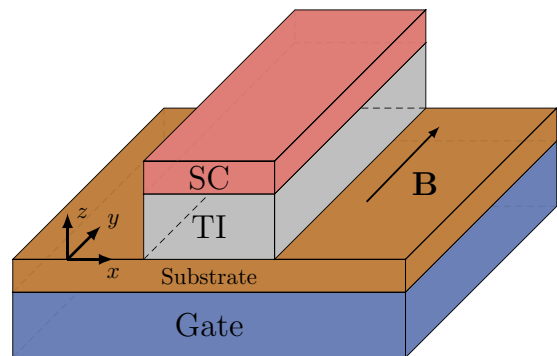
FIG. 1. *Gated TI wire.* A metallic gate (blue) induces a nonuniform chemical potential across the TI wire of cross-sectional area $L_x \times L_z$, breaking inversion symmetry and lifting the twofold degeneracy of the surface state subbands with opposite angular momenta. When a pairing potential is proximity induced by a superconducting layer placed on top of the wire (red) and a magnetic field **B** is applied parallel to the wire axis, the system can enter into a topological superconducting phase if the flux produced by **B** exceeds a critical value.

localized zero-energy MBSs occupies an exceptionally large area in parameter space. In realistic wires, the range of chemical potential with MBSs spans several meV at relatively weak magnetic-field strengths. Our protocol therefore provides a path to realizing MBSs in present-day TI wire devices.

II. SUBBAND SPLITTING

We begin with a continuum model for the Dirac surface states of a three-dimensional TI confined to a cylindrical wire. Due to confinement, the surface states form 1D subbands labeled by half-integer angular momentum $\ell = \pm\frac{1}{2}, \pm\frac{3}{2}, \ldots$ around the wire and with an energy dispersion above the Dirac point given by (see Appendix A)

$$\epsilon_\ell(k) = \hbar v_F \sqrt{k^2 + (\ell - \varphi)^2/R^2}, \qquad (1)$$

and by $-\epsilon_\ell(k)$ below the Dirac point. Here, $2\pi R$ is the perimeter of the wire cross section, k is the momentum along the wire, v_F is the Fermi velocity, and $\varphi \equiv \Phi/\Phi_0 = B\pi R^2/\Phi_0$ is the magnetic flux induced by the magnetic field B applied along the wire in units of the fundamental flux quantum $\Phi_0 = h/e$. Inversion symmetry requires that the subbands satisfy $\varepsilon_\ell(k) = \varepsilon_\ell(-k)$ and, in the absence of a magnetic field, time-reversal symmetry enforces $\varepsilon_\ell(k) = \varepsilon_{-\ell}(-k)$ [20] (see Appendix B). Therefore, when both symmetries are present, subbands are doubly degenerate for angular momenta $\pm\ell$ at all momenta k.

We first consider the influence of the gate in the absence of magnetic fields. Since the gate is placed on only one side of the wire, the resulting electrostatic field gives rise to a nonuniform chemical potential $\mu(\theta) = \mu_0 + \delta\mu(\theta)$ across the wire cross section [15,16], where μ_0 is the average chemical potential and θ is the angle from the direction normal to the gate (i.e., from the z direction in Fig. 1. This inhomogeneous chemical potential $\delta\mu(\theta)$ breaks inversion symmetry and therefore lifts the degeneracy of the subbands at finite k. Kramers theorem requires that $k \neq 0$ subbands have opposite spins at opposite momenta and at $k = 0$ subbands remain degenerate.

More precisely, within this continuum model, one can obtain the subband splitting by expanding the inhomogeneous component of the chemical potential $\delta\mu(\theta)$ in terms of Fourier cosine harmonics $\delta\mu(\theta) = 2\sum_{n=1}^{\infty}\mu_n\cos(n\theta)$. In general, the inhomogeneous potential $\delta\mu(\theta)$ causes finite matrix elements $\mathcal{M}_{\ell\tau}^{\ell'\tau'}(k)$ between the ℓ and ℓ' subband, where $\tau = \pm$ indicates subbands above $(+)$ or below $(-)$ the Dirac point (see Appendix B) [16]. When the inhomogeneity is small we can use degenerate perturbation theory for the $\ell > 0$ and $-\ell$ subbands and label the resulting subband pair by ℓ. The $n = 2|\ell|$th Fourier component of the inhomogeneous potential $\delta\mu(\theta)$ couples these degenerate subbands and results in a splitting of subbands above the Dirac point

$$\varepsilon_\ell^\pm(k) \approx \epsilon_\ell(k) \pm \frac{\mu_{2\ell}k}{\sqrt{k^2 + (\ell/R)^2}}. \qquad (2)$$

As a result, each subband minimum moves from $k = 0$ to a new minimum at $\pm k_{so}$, which can be estimated from Eq. (2),
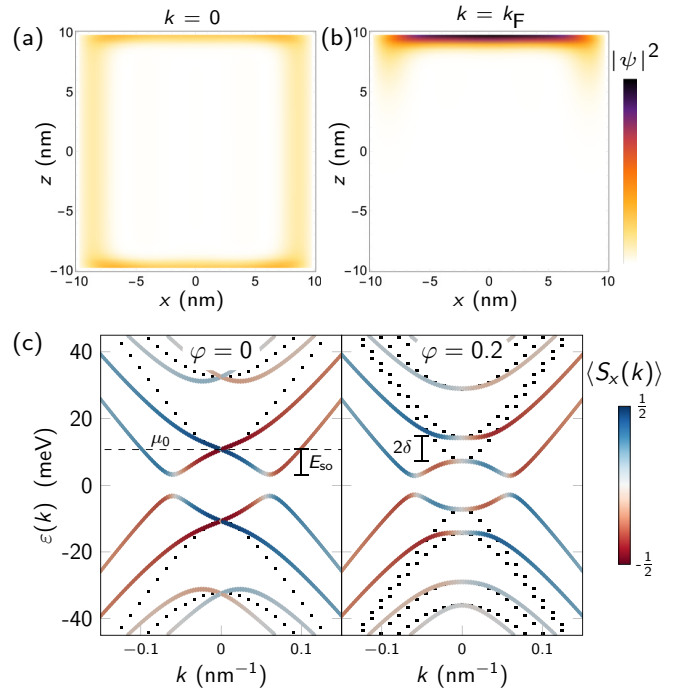
$$k_{so} \approx \mu_{2\ell}/\hbar v_F, \qquad (3)$$

FIG. 2. *Wave functions and subband splitting in gated TIs.* The energy spectrum of a 20 nm × 20 nm cross section of an infinitely long Bi$_2$Se$_3$ TI wire found numerically using the BHZ tight-binding model with the chemical-potential inhomogeneity given by $\delta\mu(z) = 3\delta\varepsilon(z/L_z)$, where z is measured from the center of the wire, and $\delta\varepsilon \approx 21$ meV (see Appendix E). (a), (b) Probability densities $|\psi_k(x,z)|^2$ in the cross section of the wire. At $k = 0$ the state remains uniformly distributed around the wire surface but at $k = k_F$ it is localized close to the top (or bottom) due to the gating. (c) The energy spectrum of the gated subbands. Colors indicate the expectation value of spin component perpendicular to the gate normal: $\langle S_x(k)\rangle = \int dx dz \langle\psi_k(x,z)|\sigma_x|\psi_k(x,z)\rangle$, where σ_i are the Pauli matrices encoding the spin in the BHZ model. (left) A large subband splitting occurs due to gating. Dotted black lines refer to subbands before gating. (right) Applying a magnetic field B along the wire opens a gap of several meV for relatively small fields due to orbital effects. For this thin wire the flux $\varphi = 0.2$ corresponds to $B \approx 2$ T and leads to a gap $2\delta(\varphi = 0.2) \approx 8$ meV.

to leading order in the inhomogeneity $\mu_{2\ell}$. The size of the splitting of a given subband pair, $E_{so}(\ell)$, is determined by the change in the subband minimal energy as

$$E_{so}(\ell) = |\epsilon_\ell(0) - \varepsilon_\ell^\pm(\pm k_{so})| \approx \frac{\mu_{2\ell}^2}{2\ell\hbar v_F/R}. \qquad (4)$$

Since inhomogeneities are typically of the order of the subband spacing $\delta\varepsilon \sim \hbar v_F/R \approx 30$ meV [15,16], the thinnest $R \approx 10$ nm experimental TI wires can achieve splitting energies $E_{so} \gtrsim 10$ meV with a corresponding length scale $l_{so} \equiv 1/k_{so} \lesssim 15$ nm. We note that this energy is a very large value when compared with the similar subband splitting caused by Rashba spin-orbit coupling in semiconducting nanowires, which is typically $E_{so} < 1$ meV in InAs or InSb [21]. We note that a further gate on top of the superconductor could be used to enable independent tuning of both μ_0 and E_{so}.

The gate-induced splitting of subbands is also confirmed numerically (see Fig. 2) by diagonalizing the Bernevig-

Hughes-Zhang (BHZ) tight-binding model Hamiltonian in momentum space for a wire with a square cross section [22–25]. To connect to realistic experimental systems throughout this paper we use parameters consistent with the TI Bi_2Se_3 [24], choosing wires with a 20 nm $\times$ 20 nm cross section and the crystallographic axes $c \| \hat{z}$ and ab-plane spanning the $\hat{x}$ and $\hat{y}$ directions [16]. As expected from our considerations above, we find that the subband splitting does not strongly depend on the exact choice of the inhomogeneity of the chemical potential and so will generically be present in any TI wire that has been gated (see Appendix E). Although a perturbative result, as seen in Fig. 2, the energy spectrum defined by Eq. (2) is still relevant even for inhomogeneities larger than the subband spacing $\delta\epsilon$. In particular, we note that the exact shape of the inhomogeneity $\delta\mu(\theta)$ induced by the gate does not influence the form of the splitting in Eq. (2) other than through the relative sizes of the harmonics $\mu_{2\ell}$. Ultimately, the magnitudes of these harmonics will depend on the wire cross section, gate geometry, and electrostatic considerations such as the screening of the superconductor, but in general splitting will be largest close to the Dirac point because the largest $\mu_{2\ell}$ will generically occur for small ℓ. From Eq. (2) we also see that there is no change in the energy at $k = 0$, which is consistent with the previous observation that such states can be connected by Klein tunneling through any chemical-potential inhomogeneity [15,16].

III. FIELD-INDUCED GAP

We now consider a magnetic field applied parallel to the wire, see Fig. 1. A magnetic field opens a gap at $k = 0$, leaving an odd number of pairs of counterpropagating modes at the Fermi level when the chemical potential is tuned close to a subband crossing [dashed line in Fig. 2(c)]. Even in the presence of the gate-induced inhomogeneity $\mu(\theta)$, due to the Klein-tunnelling effects, the wave function at $k = 0$ is uniformly distributed on the wire surface. In contrast, the wave function at k_F is localized close to the top or bottom of the wire, depending on the sign of the corresponding harmonics $\mu_{2\ell}$ [see Figs. 2(a) and 2(b)]. As a consequence, threading a magnetic flux through the gated TI wire opens a gap at $k = 0$ due to orbital effects whereas the states at finite Fermi momenta are largely unaffected by such a flux. The size of the gap is given by $\delta(\varphi) \approx \hbar v_F |\varphi|/R$ (see Appendix C). For $R \approx 10$ nm wire this means a gap of $2\delta/B \approx 4$ meV per T can be opened. In fact, δ increases linearly with wire thickness, meaning thicker wires open a gap significantly faster. For instance, a thicker $R \approx 30$ nm would open a gap of $2\delta/B \approx 12$ meV per T. In semiconductor nanowires, which use the Zeeman effect to open an equivalent gap at $k = 0$, this would require a g factor of over 200. The relevant g factor for Bi_2Se_3 is $g \approx 4$ and so the Zeeman effect in our setup is negligible compared with orbital effects [24]. Finally, we note that the surface states are spin polarized in the direction orthogonal to the wire and gate normal (the x axis in Fig. 1) and the spin expectation value in the other two directions is zero, $\langle S_y \rangle = \langle S_z \rangle = 0$. Therefore if the chemical potential is tuned inside the gap, this setup could be used as a spin-filter with nearly perfect helical modes [26–28], see Fig. 2(c).
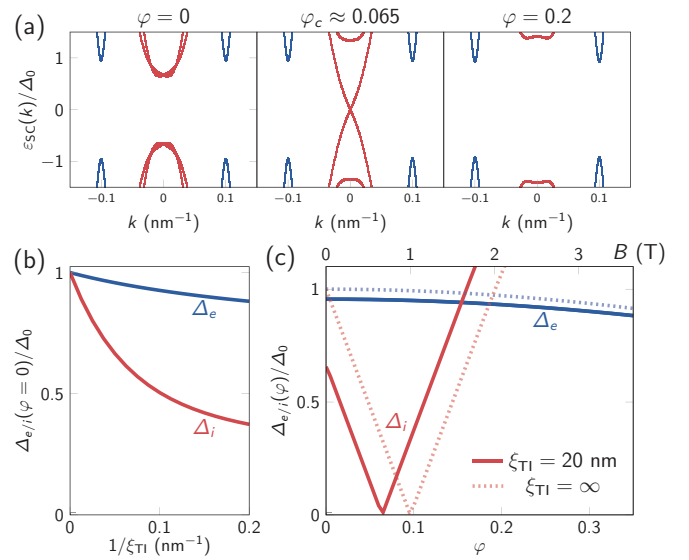

FIG. 3. *Superconductivity in a gated TI nanowire.* (a) Energy spectrum of the gated TI wire from Fig. 2 in the presence of the proximity-induced superconductivity of the strength $\Delta_0 \approx 1.6$ meV with a coherence length $\xi_{TI} = 20$ nm, consistent with the proximity effects in Bi_2Se_3 thin films due to Nb [29]. (b) The interior superconducting gap Δ_i is smaller than the exterior gap Δ_e for a finite coherence length ξ_{TI}. (c) As the magnetic field is increased the gap at $k = 0$ closes and reopens, indicating a topological phase transition [for our parameters phase transition occurs at $\varphi_c \approx 0.065$ ($B \approx 650$ mT)]. The exterior gap $\Delta_e \simeq \Delta_0$ stays almost constant. We do not take into account the field dependence of the pairing amplitude and fix $\mu = 0$.

From the above considerations, we see that, for our protocol, there is a trade-off between the size of the gap opening at a given field (larger in thicker wires) and the size of the subband splitting (larger in thinner wires). For Bi_2Se_3 and related TI materials the ideal radius R will likely lie in the range 10–30 nm. In our numerics, we use a 20 nm $\times$ 20 nm cross section ($R \approx 11.3$ nm) at the lower end of this range since smaller cross sections are numerically more accessible but this likely exaggerates the magnetic-field strengths required for the topological phase. In what follows we focus on the lowest electron subbands $\ell = \pm 1/2$ and measure μ from the subband crossing at $k = 0$. That said, our conclusions remain generally applicable also to higher energy subbands as long as the chemical-potential inhomogeneity is strong enough, a fact that may prove useful since the screening of the superconductor will limit the range of average chemical potentials μ_0 accessible in real experiments.

IV. TOPOLOGICAL SUPERCONDUCTIVITY

The remaining ingredient required for the appearance of MBSs is a proximity-induced superconductivity. We focus on the setup in which an s-wave superconductor is placed on the top of the wire and, therefore, the pairing amplitude Δ is not expected to possess a vortex [20]. A simple model for the spatial dependence of the pairing amplitude in such a setup is given by $\Delta(z) = \Delta_0 e^{-(L_z/2-z)/\xi_{TI}}$ [29], where

ξ_{TI} is the superconducting (SC) coherence length in the TI. We do not model the reduction of the pairing amplitude by magnetic field but in real systems such an effect will favor thicker wires with a larger gap $\delta(\varphi)$ at a given magnetic field (see above).

Next, we first diagonalize the BHZ tight-binding model Hamiltonian in momentum space (see Appendix F), where we include the pairing terms of the strength Δ (see Fig. 3). To achieve a large superconducting gap, the sign of the chemical-potential harmonic μ_1 must be such that the state at $k = \pm k_F$ is localized close to the superconductor. In this case, the exterior superconducting gap Δ_e, defined around $k = \pm k_F$ [shown in blue in Fig. 3(a)], is essentially unchanged by magnetic field, $\Delta_e(\varphi) \simeq \Delta_0$. On the other hand, the interior gap Δ_i, defined around $k = 0$ [shown in red in Fig. 3(a)] is smaller, $\Delta_i(\varphi = 0) < \Delta_0$, even in the absence of magnetic fields. This can be explained by the fact that the wave functions at finite Fermi momenta are located close to the superconductor, see Fig. 2(b). The amount by which $\Delta_i(\varphi = 0)$ is reduced from Δ_0 depends on the coherence length ξ_{TI} [see Fig. 3(b)]. As the magnetic field is increased, Δ_i closes and then reopens, quickly exceeding its zero-field value [see Fig. 3(c)]. The closing and reopening of the gap with magnetic field indicates the onset of a topological superconducting phase. The value φ_c at which the superconducting gap closes is found from the following condition (see Appendix D):

$$\delta^2(\varphi_c) = \mu_0^2 + \Delta_i^2(\varphi = 0). \tag{5}$$

We note that a finite coherence length, which is responsible for smaller values of Δ_i without diminishing Δ_e, allows one to enter the topological phase at weaker magnetic fields. Finally, we note that our mechanism is different from previous proposals without a vortex in various 2D TI devices [30,31].

V. MAJORANA BOUND STATES

To study properties of MBSs in the topological phase we calculate the energy spectrum of a finite wire (see Appendix F) and obtain the topological phase diagram, see Fig. 4. The white dashed line in Fig. 4(a) indicates the topological phase-transition line obtained in Eq. (5). Inside the topological phase, the MBSs are localized at the ends of the wire and pinned to zero energy, being well separated from the bulk superconducting states. Close to the phase-transition line, the MBSs overlap and split away from zero energy. Thus, generally, the zero-energy MBSs can be observed only if the localization length of MBS $\xi(\varphi)$, determined by the smallest gap in the spectrum, is smaller than the half of the wire length L_y such that the following criteria is satisfied [32]:

$$\xi(\varphi) = \frac{\hbar v_F}{\min\{\Delta_i(\varphi), \Delta_e(\varphi)\}} \lesssim L_y/2. \tag{6}$$

This transition line is indicated by the red dashed line in Fig. 4(a). The well-localized zero-energy MBSs persist for a large region of phase space spanning several meV of average chemical potential for fixed finite B fields. As a consequence, MBSs are robust against large local fluctuations of chemical potential caused by disorder (see Appendix G). In stark contrast, without the nonuniformity of chemical potential and
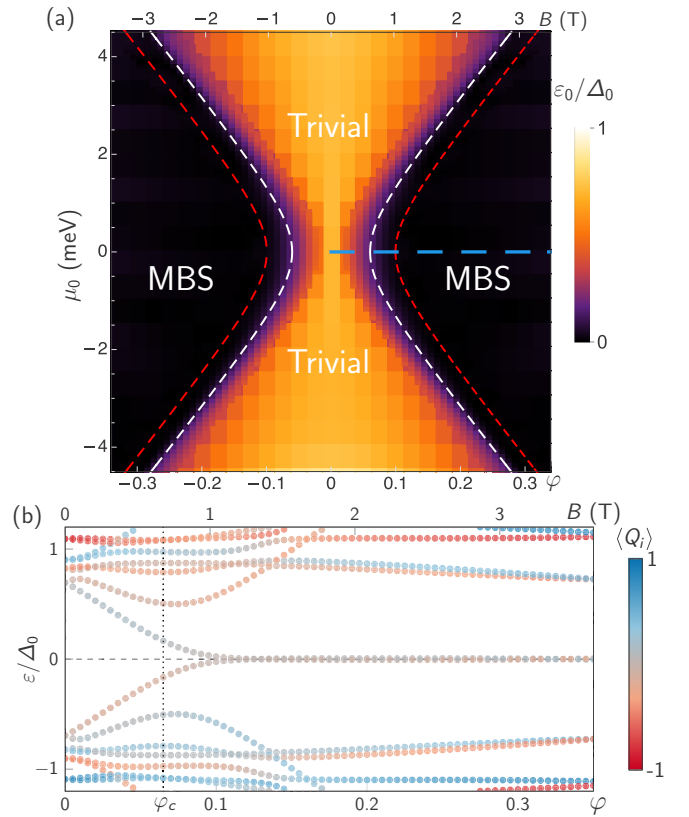

(a)

(b)

FIG. 4. *MBSs in a finite gated TI wire without a vortex.* The same TI wire as in Fig. 3 but of a finite 1000 nm length. (a) The lowest-energy eigenstates as a function of (average) chemical potential μ_0 and flux φ. The topological phase transition (white dashed line) corresponds to the closing of the interior bulk gap defined in momentum space. Inside the topological phase (beyond the red dashed line), zero-energy MBSs (black) are well separated from the bulk superconducting states, whereas close to the topological phase-transition line, their localization length is comparable with the wire length such that they split away from zero energy. (b) The lowest part of the energy spectrum [taken along the blue dashed line of panel (a)], where colors indicate the BCS charge $\langle Q_i \rangle = \int d^3r \langle \psi_i(\boldsymbol{r})| \eta_3 |\psi_i(\boldsymbol{r})\rangle$, with η_i being the Pauli-matrices in particle-hole space [25]. Zero-energy chargeless MBSs appear in the topological phase when the condition on the localization length is fulfilled [see Eq. (6)], which for this thin wire happens for a flux $\varphi \approx 0.1$ ($B \approx 1$ T) which is a bit larger than $\varphi_c \approx 0.065$ ($B = 650$ mT) where the interior bulk gap closes, see Fig. 3.

with no vortex in the pairing potential, the localization-length condition of Eq. (6) would not be satisfied for any position in phase space.

VI. CONCLUSIONS

We have shown that it is possible to generate Majorana bound states in topological insulator wires without the requirement of a vortex thanks to a large subband splitting of the 1D surface states arising due to a nonuniform chemical potential across the wire cross-section induced by a gate. In our setup, the topological phase occupies a large region of parameter space and MBSs are robust against disorder. Since a vortex is not required in our protocol it opens a path to MBSs in state-of-the-art TI wire devices.

APPENDIX A: SUBBANDS AND SYMMETRIES OF TOPOLOGICAL INSULATOR WIRE WITHOUT GATING

A continuum model for the Dirac surface states confined to a cylindrical wire of radius R has been considered in previous studies of TI wires [9,18,20,33–35] and we follow a similar derivation in this section. The general Hamiltonian describing TI states confined to the surface with normal $\boldsymbol{n}$ is given by [34]

$$H_{\text{surf}} = \frac{\hbar v_F}{2} \boldsymbol{\nabla} \cdot \boldsymbol{n} + \frac{v_F}{2}[\boldsymbol{n} \cdot (\boldsymbol{p} \times \boldsymbol{\sigma}) + (\boldsymbol{p} \times \boldsymbol{\sigma}) \cdot \boldsymbol{n}], \quad \text{(A1)}$$

where the momentum operator is $\boldsymbol{p} = -i\hbar\boldsymbol{\nabla}$ and $\boldsymbol{\sigma} = (\sigma_x, \sigma_y, \sigma_z)$ is the vector of Pauli matrices, with σ_i acting in spin space. This Hamiltonian describes a helical system with the spin states being perpendicular to the momentum and normal $\boldsymbol{n}$. For the case of a cylinder along $\hat{\boldsymbol{y}}$ we can write the normal as $\boldsymbol{n} = (\sin\theta, 0, \cos\theta)$ where θ is the angle from the $\hat{z}$ direction. The Hamiltonian of the surface states of such a cylindrical TI wire is given by

$$H(y, \theta) = \frac{\hbar v_F}{2R} + i\hbar v_F \boldsymbol{n} \cdot (\boldsymbol{\sigma} \times \boldsymbol{\nabla})$$
$$= \frac{\hbar v_F}{2R} - i\hbar v_F \left[\sigma_y \frac{\partial_\theta}{R} - (\cos\theta\sigma_x - \sin\theta\sigma_z)\partial_y\right], \quad \text{(A2)}$$

where we used $\boldsymbol{\nabla} \times \boldsymbol{n} = 0$ and $\partial_\theta/R = \cos\theta\partial_x - \sin\theta\partial_z$. The solutions are 2π periodic in the angle θ. The constant term $\frac{\hbar v_F}{2R}$ arises for energies measured from the Dirac point [35]. Solutions to $H(y, \theta)$ can be found by applying the unitary transformation $U(\theta) = e^{i\theta\sigma_y/2}$ which transforms $H(y, \theta)$ to the simple form

$$\bar{H}(y, \theta) \equiv U(\theta)H(y, \theta)U^\dagger(\theta)$$
$$= -i\hbar v_F\left(\sigma_y \frac{\partial_\theta}{R} - \sigma_x \, \partial_y\right). \quad \text{(A3)}$$

Since the transformation satisfies $U(\theta) = -U(\theta + 2\pi)$, the boundary conditions for θ of the eigenstates of the transformed Hamiltonian $\bar{H}(y, \theta)$ are 2π antiperiodic. We note at this point that the above discussion would be unaffected by the introduction of a nonuniform potential $\delta\mu(\theta)$ since the transformation $U(\theta)$ has no effect on it. Similarly, a Zeeman term $\frac{1}{2}g\mu_B B\sigma_y$ for a magnetic field B parallel to the wire (see below) would also be unaffected by this transformation.

The solutions of the transformed Hamiltonian of Eq. (A3) have a simple plane-wave form (up to normalization)

$$\psi_{k\ell\tau}(y, \theta) = \chi_{k\ell\tau}e^{i(ky+\ell\theta)}, \quad \text{(A4)}$$

where k is the momentum along the wire, $\chi_{k\ell\tau}$ is the spinor encoding the chirality, $\tau = \pm$ indicates whether the state is above or below the Dirac point, and $\ell = \pm\frac{1}{2}, \frac{3}{2}, \ldots$ is the angular momentum around the wire, which is a half integer

due to the antiperiodic boundary conditions in θ. As in Eq. (1) of the main text, above the Dirac point ($\tau = +$), these states have energies

$$\varepsilon_\ell(k) = \hbar v_F\sqrt{k^2 + (\ell/R)^2}, \quad \text{(A5)}$$

and below the Dirac point ($\tau = -$) have energies $-\varepsilon_\ell(k)$. The spacing between subbands is given by $\delta\varepsilon = \hbar v_F/R$. The normalized eigenspinors are given by

$$\chi_{k\ell\tau} = \frac{1}{\sqrt{2}}\left(\tau, \frac{i\ell/R - k}{\sqrt{k^2 + (\ell/R)^2}}\right). \quad \text{(A6)}$$

APPENDIX B: MATRIX ELEMENTS DUE TO NONUNIFORM CHEMICAL POTENTIAL

The Hamiltonian $\bar{H}(y, \theta)$ describing surface states of the TI wire [see Eq. (A3)] has an inversion symmetry of the full three-dimensional space, i.e., $\bar{H}(y, \theta) = \sigma_y\bar{H}(-y, \theta + \pi)\sigma_y$, which enforces that the energies satisfy $\varepsilon_\ell(k) = \varepsilon_\ell(-k)$. This inversion symmetry is broken by the nonuniform chemical potential $\delta\mu(\theta)$ induced by the gate. The system also has a time-reversal symmetry, $\bar{H}(y, \theta) = \sigma_y\bar{H}^*(y, \theta)\sigma_y$, which requires $\varepsilon_\ell(k) = \varepsilon_{-\ell}(-k)$. The combination of these symmetries ensures degeneracy of the subbands for all momenta k [20] (see Fig. 5).

When inversion symmetry is broken by a nonuniform chemical potential $\delta\mu(\theta)$, matrix elements $\mathcal{M}_{\ell\tau}^{\ell'\tau'}(k)$ are induced which connect states with different angular momenta ℓ and ℓ' for potentially different τ and τ'. These matrix elements result in a subband splitting, as discussed in the main text. To obtain this splitting analytically, we start with the general form of the matrix elements between the eigenstates $\psi_{k\ell\tau}$ and $\psi_{k'\ell'\tau'}$, which are given by

$$\mathcal{M}_{\ell\tau}^{\ell'\tau'}(k) = \langle\psi_{k\ell\tau}|\,\delta\mu\,|\psi_{k\ell'\tau'}\rangle$$
$$= \chi_{k\ell\tau}^\dagger\chi_{k\ell'\tau'}\int_0^{2\pi}\frac{d\theta}{2\pi}e^{i(\ell'-\ell)\theta}\delta\mu(\theta)$$
$$= \frac{\mu_{|\ell-\ell'|}}{2}\left(\tau\tau' + \frac{(k + i\ell/R)(k - i\ell'/R)}{\sqrt{k^2 + (\ell/R)^2}\sqrt{k^2 + (\ell'/R)^2}}\right), \quad \text{(B1)}$$

where in the final line $\ell \neq \ell'$. As in the main text, μ_n is the nth Fourier cosine component, $\delta\mu(\theta) = 2\sum_{n=1}^\infty \mu_n\cos(n\theta)$, where the geometry of our setup means that the nonuniform potential is equal for the two points (x, z) and $(-x, z)$ on the TI surface or, equivalently, $\delta\mu(\theta) = \delta\mu(-\theta)$.

Taking $\ell > 0$, in the special case of the degenerate subbands $\ell' = -\ell$ with $\tau = \tau'$, this matrix element reduces to

$$\mathcal{M}_{\ell\tau}^{-\ell\tau}(k) = \frac{\mu_{2\ell}k}{k - i\ell/R}. \quad \text{(B2)}$$

Assuming that the maximum size of all μ_n is much smaller than the subband spacing $\delta\varepsilon$, we can use degenerate perturbation theory to find the energy spectrum. For the bands above the Dirac point, this gives

$$\varepsilon_\ell^\pm(k) \approx \varepsilon_\ell(k) \pm \frac{\mu_{2\ell}k}{\sqrt{k^2 + (\ell/R)^2}}, \quad \text{(B3)}$$
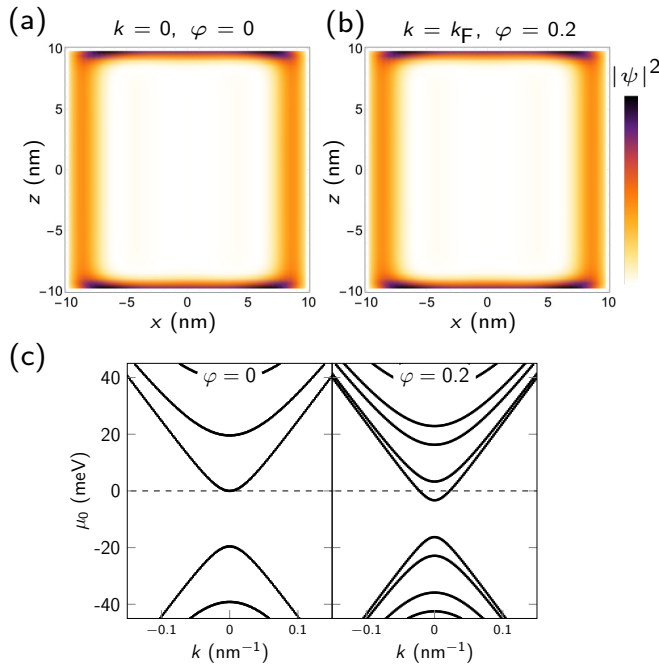
FIG. 5. *Wave functions and energy spectrum for a TI wire with uniform chemical potential.* The same wire as in Fig. 2 of the main text but without the nonuniformity in the chemical potential. Here, in addition, the bottom of the lowest subband is tuned to zero energy. (a), (b) In stark contrast with a gated wire (see Fig. 2 of the main text) the wave functions are not localized on a specific side of the TI wire at finite k_F. (c) The subbands of the TI wire with a uniform chemical potential are doubly degenerate for $\varphi = 0$ and have an energy spacing $\delta\varepsilon \approx 21$ meV.

and similarly $-\varepsilon_\ell^\pm(k)$ below the Dirac point [as in Eq. (3) of the main text]. We find that such splitting between the two degenerate subbands is present for a general form of chemical potential inhomogeneities $\delta\mu(\theta)$ (see Fig. 6) and
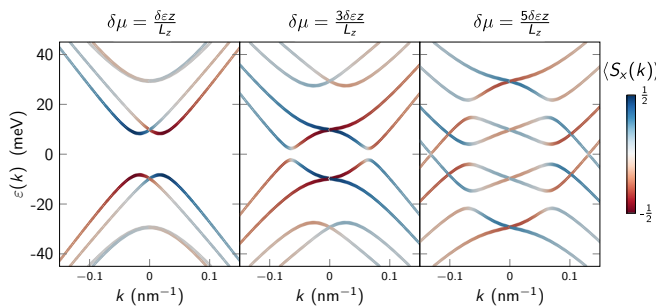

FIG. 6. *Band splittings for different strengths of nonuniform potential.* The energy spectrum of a Bi$_2$Se$_3$ wire with a 20 nm × 20 nm cross section for three different strengths of nonuniformity of chemical potential $\delta\mu$ calculated using the BHZ tight-binding model for a wire in momentum space [see Eq. (E1)]. We find that the perturbative result for the band splitting given in Eq. (B3) is valid for large values of the inhomogeneity $\delta\mu(\theta)$, even when it is larger than the subband spacing $\delta\varepsilon \approx 21$ meV and only deviates from the perturbative result when the splitting energy of a given subband is too large, $E_{so} \gtrsim \delta\varepsilon/2$.
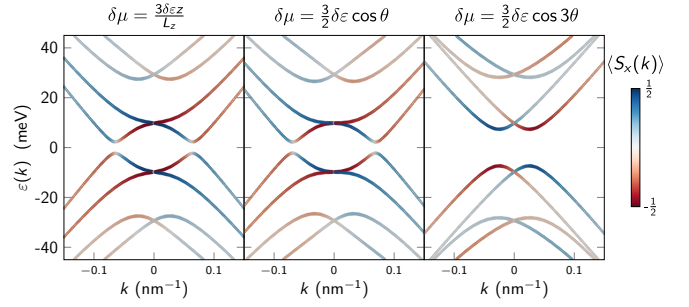

FIG. 7. *Band splittings for different shapes of nonuniform potential.* The energy spectrum of a Bi$_2$Se$_3$ wire with a 20 nm × 20 nm cross section for three different nonuniformities of chemical potential, calculated using the BHZ tight-binding model for a wire in momentum space [see Eq. (E1)]. The exact shapes of nonuniform potentials used are listed at the top of the panels. The subband spacing is $\delta\varepsilon \approx 21$ meV and the angle θ is taken from the $\hat{z}$ direction. As expected from our analytical calculations, two shapes of nonuniform part of the chemical potential, $\delta\mu = \frac{3\delta\varepsilon z}{L_z}$ and $\delta\mu = \frac{3}{2}\delta\varepsilon\cos\theta$, result in similar values of the splitting for the lowest-angular-momentum subbands. In contrast with that, for $\delta\mu = \frac{3}{2}\delta\varepsilon\cos 3\theta$, the splitting is weaker for the lowest $\ell = \pm 1/2$ subbands than in the first two cases, as also can be expected from our analytical treatment.

not strongly dependent on the exact form of inhomogeneity (see Fig. 7 and discussion below). The momentum $\pm k_{so}$ of the band minimum can be found by solving $\partial_k\varepsilon_\ell^\pm(k)|_{k_{so}} = 0$. One also obtains the size of the subband splitting defined as $E_{so}(\ell) = |\epsilon_\ell(0) - \varepsilon_\ell^\pm(\pm k_{so})|$. Expansion of k_{so} and E_{so} to leading order in $\mu_{2\ell}$ gives Eqs. (4) and (5) of the main text, respectively.

We note that, it is the nonuniform chemical potential $\delta\mu(\theta)$ that leads to the subband splitting and not the electric field itself. For a given TI wire device, to obtain the potential $\delta\mu(\theta)$, one needs to consider the electrostatics of the device [15]. In general, $\delta\mu(\theta)$ is a result of both a nonuniformity in charge density, related to the geometric capacitance of the wire, and the direct electrostatic potential, related to the quantum capacitance of the wire. Far from the Dirac point the charge density is most important but quantum capacitance effects can become relevant in the low-density region close to the Dirac point. In the setup as shown in Fig. 1 of the main text, the adjustment of the uniform chemical potential μ_0 is not entirely independent of the nonuniform $\delta\mu(\theta)$, however, it is likely that one will always need to apply some gate voltage to tune μ_0 close to a band crossing point. As stated in the main text, an additional gate on top of the superconductor can enable a more independent tuning of the uniform chemical potential μ_0 and the nonuniform chemical potential $\delta\mu(\theta)$ if required.

APPENDIX C: MAGNETIC FIELD PARALLEL TO THE WIRE

A magnetic field applied parallel to the wire (along the $\hat{y}$ axis in our coordinate system), generally, leads to both orbital and Zeeman contributions to the Hamiltonian. An additional Zeeman term $H_Z = \frac{1}{2}g_\parallel\mu_B B\sigma_y$ added to the Hamiltonian (A2)

will be unaffected by the unitary transformation $U(\theta)$ we used to derive $\bar{H}(y, \theta)$. This is also true for the orbital component which can be included by minimal coupling, $\boldsymbol{p} \to \boldsymbol{p} - e\boldsymbol{A}$, with the vector potential $\boldsymbol{A}$ in Eq. (A2). Using the symmetric gauge $\boldsymbol{A} = B/2(z, 0, -x) = \frac{\hbar\varphi}{eR}(\cos\theta, \ 0, \ -\sin\theta)$—which is also unaffected by $U(\theta)$—allows us to write

$$\bar{H}(y, \theta) + H_Z = \hbar v_F \left[\sigma_y \left(\frac{-i\partial_\theta - \varphi}{R} + \frac{g_\parallel \mu_B B}{2\hbar v_F} \right) + i\sigma_x \partial_y \right],$$
(C1)

where $\Phi = \pi R^2 B$ is the magnetic flux through the wire, with $\varphi = \Phi/\Phi_0$ being the dimensionless flux phase and $\Phi_0 = h/e$ the flux quantum, as in the main text. Therefore, a parallel magnetic field can be included by replacing of the angular momentum $\ell \to \lambda_\ell \equiv \ell - \varphi + \frac{\frac{1}{2} g_\parallel \mu_B B}{\hbar v_F/R}$. We note that, in this effective low-energy theory, the orbital and spin contributions of a parallel magnetic field add up to one term with the orbital term usually being dominant [36].

As discussed in the main text, the field lifts the degeneracy of the modes at $k = 0$. To find the size of the gap, we can solve the Hamiltonian for a TI wire surface in the presence of a magnetic field, Eq. (C1), using the wave functions $\psi_{k\lambda_\ell\tau}(y, \theta)$ from Eq. (A4), where we have replaced $\ell \to \lambda_\ell$. The energy spectrum is given by $\pm\varepsilon_{\lambda_\ell}(k)$ above ($+$) and below ($-$) the Dirac point. At $k = 0$, the gap is given by

$$\delta(\varphi) = |\varepsilon_{\lambda_\ell}(0) - \varepsilon_{\lambda_{-\ell}}(0)|/2 = \hbar v_F |\lambda_\ell - \lambda_{-\ell}|/2R$$
$$= |2\hbar v_F \varphi/R - g_\parallel \mu_B B|/2 \approx \hbar v_F |\varphi|/R, \quad (C2)$$

where the approximation uses the fact the Zeeman contribution is typically much smaller than the orbital flux contribution. For instance, in the ab plane of Bi_2Se_3 the g factor is $g_\parallel \approx 4$ and hence the Zeeman contribution $g_\parallel \mu_B \approx 0.2$ meV/T can be safely neglected in comparison with the orbital contribution $2\hbar v_F |\varphi|/R \gtrsim 4$ meV/T. In tight-binding models (see below) and real systems the finite penetration of the wave function into the TI cross section requires that φ be replaced by the effective flux $\bar{\varphi}$ that, for example, governs the Aharonov-Bohm period and is slightly smaller than φ. For our parameters and our 20 nm × 20 nm cross section, $\bar{\varphi} \approx 5\varphi/6$.

Next, we show that the size of the splitting between two initially degenerate subbands at $k = 0$ induced by the magnetic field stays the same even if the nonhomogeneity of the chemical potential is included. The matrix elements between *different* subbands $\mathcal{M}_{\lambda_\ell\tau}^{\lambda_{\ell'}\tau'}(k = 0)$ are given by

$$\mathcal{M}_{\lambda_\ell\tau}^{\lambda_{\ell'}\tau'}(k = 0) = \frac{\mu_{|\ell-\ell'|}}{2}[\tau\tau' + \text{sgn}(\lambda_\ell\lambda_{\ell'})]. \quad (C3)$$

We focus on the case of weak magnetic fields $\varphi < 1/2$ such that λ_ℓ and $\lambda_{\ell'}$ do not change sign as a function of the magnetic field. Thus, this matrix element stays equal zero between two

subbands (ℓ, τ) and $(-\ell, \tau)$ of our main interest. This means that the gap induced by the magnetic field is not altered by gating and is given by $\delta = \hbar v_F |\varphi|/R$. We confirm this numerically. For instance, in Fig. 2(c) of the main text, we show that $\delta(\varphi = 0.2)$ is essentially identical for the system with and without a nonuniform chemical potential.

APPENDIX D: TOPOLOGICAL SUPERCONDUCTIVITY TRANSITION

In this section, we derive the criterion for the critical flux φ_c that defines the phase transition to topological superconductivity. The topological superconductivity arises due to the competition between two gap-opening mechanisms at $k = 0$: namely, between the superconducting gap $\Delta_{i,\ell}$ and the magnetic field gap $\delta_\ell(\varphi)$ for a general subband ℓ. In what follows, we assume that the uniform part of the chemical potential $\mu_{0,l}$ is calculated from the degeneracy point at $k = 0$ for two subbands $\pm\ell$ and treat both $\Delta_{i,\ell}$ and $\delta_\ell(\varphi)$ perturbatively, $\delta_\ell(\varphi), \Delta_{i,\ell} \ll E_{so,\ell}$. In this case, linearizing the spectrum around $k = 0$ [see Fig. 2(c) in the main text], the effective low-energy Hamiltonian for the two interior modes $R_{i,\ell}(y)$ (right-moving field) and $L_{i,\ell}(y)$ (left-moving field) can be written as

$$H_\ell = \hbar \tilde{v}_{F,\ell} k \rho_z \eta_z + \Delta_{i,\ell} \eta_x + \delta_\ell(\varphi) \rho_x \eta_z - \mu_{0,\ell} \eta_z, \quad (D1)$$

where $\eta_{x,y,z}$ are the Pauli matrices in particle-hole space, and $\rho_{x,y,z}$ are the Pauli matrices acting in the right- and left-moving field space. The Fermi velocity $\tilde{v}_{F,\ell}$ around $k = 0$, for the cylindrical TI wire, is given by $\hbar \tilde{v}_{F,\ell} = |\mu_{2l}|R/\ell$. From Eq. (D1) it follows that the interior gap closes and reopens at $k = 0$ for $\delta_\ell^2(\varphi_c) = \mu_{0,\ell}^2 + \Delta_{i,\ell}^2$. This gives the criterion for the topological phase transition, as in Eq. (6) of the main text for $\ell = 1/2$.

APPENDIX E: BERNEVIG-HUGHES-ZHANG TIGHT-BINDING MODEL WITHOUT SUPERCONDUCTIVITY

We perform numerical simulations using a BHZ tight-binding model without and with a superconducting pairing term [20,22,24,25]. Electrostatic factors mean that, ultimately, the cross section of the wire and gate geometry will impact the relative sizes of the Fourier harmonics, for instance a hexagonal cross section would result in a large μ_6 Fourier component [16]. That said, from our analytic treatment we do not expect the cross section to impact the form of the splitting for a given subband other than through the differing μ_n and so we choose a square cross section for our numerical calculations throughout. That we find subband splittings for square-cross-section wire that are consistent with our analytic calculations for a perfect cylindrical wire further validates the fact that the exact cross section of a given wire is essentially irrelevant as long as the harmonics μ_n of the nonuniform chemical potential are the same. We start with the BHZ lattice model of the TI wire with the cross section $L_x \times L_z$ in the absence of superconductivity. In momentum space, the Hamiltonian is defined as [20,22,24,25]

$$H(k) = \sum_{n=1,m=1}^{L_x/a_1, L_z/a_3} \mathbf{c}_{n,m,k}^\dagger \cdot \left\{ M(k)\tau_z + \frac{A_2}{a_2}\sin(ka_2)\tau_x\sigma_x - \mu_{n,m} \right\} \mathbf{c}_{n,m,k}$$

$$+ \sum_{n=1,m=1}^{L_x/a_1-1, L_z/a_3} \left[\mathbf{c}_{n+1,m,k}^\dagger \cdot \left\{ \frac{B_1}{a_1^2}\tau_x + \frac{iA_1}{2a_1}\tau_x\sigma_z \right\} e^{i\phi_m^x}\mathbf{c}_{n,m,k} + \text{H.c.} \right] + \sum_{n=1,m=1}^{L_x/a_1, L_z/a_3-1} \left[\mathbf{c}_{n,m+1,k}^\dagger \cdot \left\{ \frac{B_3}{a_3^2}\tau_x + \frac{iA_3}{2a_3}\tau_y \right\} e^{i\phi_n^z}\mathbf{c}_{n,m,k} + \text{H.c.} \right],$$

$$(E1)$$

where $M(k) = M_0 - 2\frac{B_2}{a_2^2}\cos(ka_2) + 2(\frac{B_1}{a_1^2} + \frac{B_2}{a_2^2} + \frac{B_3}{a_3^2})$, with A_i and B_i, $i = 1, 2, 3$, being the BHZ parameters. Here, $\mathbf{c}_{n,m,k}^\dagger = (c_{+,\uparrow}^\dagger, c_{-,\uparrow}^\dagger, c_{+,\downarrow}^\dagger, c_{-,\downarrow}^\dagger)_{n,m,k}$ is a four-vector with $c_{\pm,\uparrow/\downarrow}^\dagger$ describing the creation of an electron $+$ (hole $-$) with spin $\uparrow/\downarrow$ on site $n = x/a_1$, $m = z/a_3$ and with momentum k along the wire axis in the y direction. The Pauli matrices $\tau_{x,y,z}$ act in electron-hole space and $\sigma_{x,y,z}$ in spin space. The Peierls phases ϕ_m^x and ϕ_n^z encode the orbital component of the magnetic field B, as above (and also in Ref. [20]) we choose the symmetric gauge $A = \frac{B}{2}(z, 0, -x)$ with the origin corresponding to the center of the wire. Explicitly, this means we choose the Peierls phases as

$$\phi_m^x = \frac{a_1\pi\varphi}{L_x L_z}\left[a_3\left(m - \frac{1}{2}\right) - \frac{L_z}{2} \right], \quad (E2)$$

and

$$\phi_n^z = -\frac{a_3\pi\varphi}{L_x L_z}\left[a_1\left(n - \frac{1}{2}\right) - \frac{L_x}{2} \right], \quad (E3)$$

where now $\varphi = BL_x L_z/\Phi_0$.

Throughout we use the parameters for Bi_2Se_3 from Ref. [24] (Table IV); these are $A_1 = 3.33$ eV Å, $A_2 = \alpha 3.33$ eV Å, $A_3 = 2.26$ eV Å, $M_0 = -0.28$ eV, $B_1 = B_2 = 44.5$ eV Å^2, and $B_3 = 6.86$ eV Å^2. We always use $\alpha = 1$ for wires in momentum space but adjust α to enable simulation of long finite systems (see below) and we choose the crystallographic c axis of Bi_2Se_3 parallel to $\hat{z}$. We also always choose lattice constants $a_1 = a_2 = 50/3$ Å in the $\hat{x}$ and $\hat{y}$ directions and $a_3 = 25/3$ Å in the $\hat{z}$ direction. We find that these are the smallest values such that lattice spacing effects are negligible, this makes our 20 nm × 20 nm cross section to be modeled as a system consisting of 12 × 24 lattice sites in the xz plane. Using these parameters for our 20 nm × 20 nm cross section we find $\delta\varepsilon = 2\pi\hbar/(2L_x/v_x + 2L_z/v_z) \approx 21$ meV, which is a generalized version of $\delta\varepsilon = \hbar v_F/R$ for a square cross section with different velocities in the x and z directions. These velocities are obtained from the BHZ model parameters

using $v_x = A_1/\hbar$ and $v_z = A_3/\hbar$. As shown in Fig. 5, when the chemical potential is uniform, the wave function is also uniformly around the wire surface for both Fermi momenta at $k = 0$ and at $k = \pm k_F$. This is very different than the gated TI wire, in which, for finite Fermi momenta, the wave function is more localized on one side of the wire (see Fig. 2 in the main text).

We use this model to confirm the validity of our perturbative solution for the size of the band splitting between two degenerate subbands as outlined in Eq. (B3), see Fig. 6. We calculate the energy spectrum for three different strengths of the nonuniform part of the chemical potential: $\delta\mu(z) = n\delta\varepsilon z/L_z$ with $n = 1, 3, 5$. We find that Eq. (B3) stays valid even when the applied bias is larger than the subband spacing $\delta\varepsilon$ and deviates from the perturbative result only when the splitting energy of a given subband gets too large $E_{\text{so}} \gtrsim \delta\varepsilon/2$.

To confirm that the splitting between degenerate subbands described by Eq. (B3) is not strongly dependent on the exact form of the inhomogeneity of chemical potential and is only sensitive to the relative sizes of the harmonics μ_n, we consider three different chemical-potential profiles $\delta\mu(z)$: $3\delta\varepsilon z/L_z$ (as in the main text), $\frac{3}{2}\delta\varepsilon\cos\theta$, and $\frac{3}{2}\delta\varepsilon\cos 3\theta$, with $\theta = \arctan(x/z)$. The results are shown in Fig. 7. As expected, for the first two chemical-potential profiles we find virtually no difference between the magnitude of splitting for the lowest subbands. For the third profile, the splitting is smaller for $\ell = \pm 1/2$ subbands than in the first two cases but approximately the same for $\ell = \pm 3/2$, as expected from our analytic treatment. In all cases, the splitting is well described by Eq. (B3).

APPENDIX F: SUPERCONDUCTING BERNEVIG-HUGHES-ZHANG MODEL

Next, we add an on-site pairing amplitude $\Delta_{n,m}$, induced by proximity to an s-wave superconductor, to the Hamiltonian in momentum space defined by Eq. (E1) and obtain

$$H_{\text{sc}}(k) = \sum_{n=1,m=1}^{L_x/a_1, L_z/a_3} \bar{\mathbf{c}}_{n,m,k}^\dagger \cdot \left[\left\{ M(k)\tau_z + \frac{A_2}{a_2}\sin(ka_2)\tau_x\sigma_x - \mu_{n,m} \right\}\eta_z + \Delta_{n,m}\eta_x \right]\bar{\mathbf{c}}_{n,m,k}$$

$$+ \sum_{n=1,m=1}^{L_x/a_1-1, L_z/a_3} \left[\bar{\mathbf{c}}_{n+1,m,k}^\dagger \cdot \left\{ \frac{B_1}{a_1^2}\tau_z + \frac{iA_1}{2a_1}\tau_x\sigma_z \right\}\eta_z e^{i\eta_z\phi_m^x}\bar{\mathbf{c}}_{n,m,k} + \text{H.c.} \right]$$

$$+ \sum_{n=1,m=1}^{L_x/a_1, L_z/a_3-1} \left[\bar{\mathbf{c}}_{n,m+1,k}^\dagger \cdot \left\{ \frac{B_3}{a_3^2}\tau_z + \frac{iA_3}{2a_3}\tau_y \right\}\eta_z e^{i\eta_z\phi_n^z}\bar{\mathbf{c}}_{n,m,k} + \text{H.c.} \right], \quad (F1)$$

where $\Delta_{n,m} = \Delta_0 e^{(ma_3 - L_z)/\xi_{TI}}$ is the proximity-induced pairing amplitude. We have introduced the extra set of Pauli matrices η_x, η_y, η_z that act in particle-hole space of the Nambu operator and we have defined

$$\bar{\mathbf{c}}^{\dagger}_{n,m,k} = (c^{\dagger}_{+,\uparrow}, c^{\dagger}_{-,\uparrow}, c^{\dagger}_{+,\downarrow}, c^{\dagger}_{-,\downarrow}, c_{+,\downarrow}, c_{-,\downarrow}, -c_{+,\uparrow}, -c_{-,\uparrow})_{n,m,k} \tag{F2}$$

in this space. This superconducting BHZ model defined in momentum space is used for Fig. 3 of the main text.

To realize MBSs at the end of the wire as in Fig. 4 of the main text, we perform the full three-dimensional BHZ tight-binding model simulations:

$$
\begin{aligned}
H_{\mathrm{obc}} = {} & \sum_{l=1,n=1,m=1}^{L_y/a_2,L_x/a_1,L_z/a_3} \bar{\mathbf{c}}^{\dagger}_{l,n,m} \cdot [\{M\tau_z - \mu_{n,m}\}\eta_z + \Delta_{n,m}\eta_x]\bar{\mathbf{c}}_{l,n,m} + \sum_{l=1,n=1,m=1}^{L_y/a_2-1,L_x/a_1,L_z/a_3} \left[\bar{\mathbf{c}}^{\dagger}_{l+1,n,m} \cdot \left\{ \frac{B_2}{a_2^2}\tau_z + \frac{iA_2}{2a_2}\tau_x\sigma_x \right\}\eta_z \bar{\mathbf{c}}_{l,n,m} + \mathrm{H.c.} \right] \\
& + \sum_{l=1,n=1,m=1}^{L_y/a_2,L_x/a_1-1,L_z/a_3} \left[\bar{\mathbf{c}}^{\dagger}_{l,n+1,m} \cdot \left\{ \frac{B_1}{a_1^2}\tau_z + \frac{iA_1}{2a_1}\tau_x\sigma_z \right\}\eta_z e^{i\eta_z\phi_m^x}\bar{\mathbf{c}}_{l,n,m} + \mathrm{H.c.} \right] \\
& + \sum_{l=1,n=1,m=1}^{L_y/a_2,L_x/a_1,L_z/a_3-1} \left[\bar{\mathbf{c}}^{\dagger}_{l,n,m+1} \cdot \left\{ \frac{B_3}{a_3^2}\tau_z + \frac{iA_3}{2a_3}\tau_y \right\}\eta_z e^{i\eta_z\phi_n^z}\bar{\mathbf{c}}_{l,n,m} + \mathrm{H.c.} \right],
\end{aligned} \tag{F3}
$$

with $M = M_0 + 2(\frac{B_1}{a_1^2} + \frac{B_2}{a_2^2} + \frac{B_3}{a_3^2})$ and the operators defined in the Nambu space as

$$\bar{\mathbf{c}}^{\dagger}_{l,n,m} = (c^{\dagger}_{+,\uparrow}, c^{\dagger}_{-,\uparrow}, c^{\dagger}_{+,\downarrow}, c^{\dagger}_{-,\downarrow}, c_{+,\downarrow}, c_{-,\downarrow}, -c_{+,\uparrow}, -c_{-,\uparrow})_{l,n,m}. \tag{F4}$$

To easily numerically simulate real system sizes of Bi_2Se_3, such as our 20 nm $\times$ 20 nm $\times$ 1000 nm wire, while also minimizing lattice effects, we adjust the Fermi velocity parallel to the wire which reduces the number of sites required along the wire. This is done via α in the parameter $A_2 = \alpha 3.33$ eV Å of our BHZ model. For the phase diagram in Fig. 4(a) and the disordered wires in the next section we choose $\alpha = 1/5$ such that wires are $12 \times 24 \times 100$ lattice sites and for Fig. 4(b) we choose $\alpha = 10/3$ such that wires are $12 \times 24 \times 150$ lattice sites. This change in A_2 (or equivalently the Fermi velocity $A_2/\hbar$) from the value with $\alpha = 1$ has no influence on our results.

When the topological criterion of the main text is fulfilled, the lowest-energy states, MBSs, are close to zero in energy and are well localized (see Fig. 8). The probability densities of the MBS wave functions along the wire, summed over the
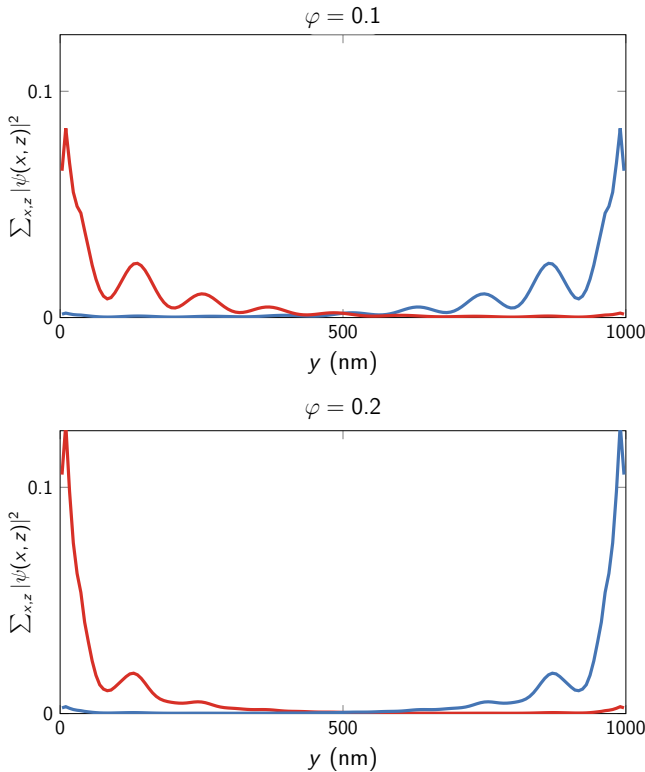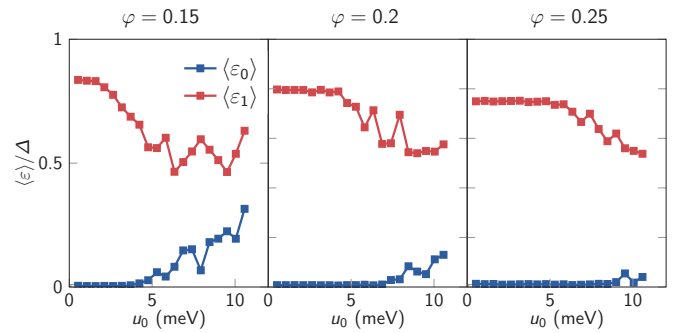

FIG. 8. *Probability densities of MBSs along the wire.* The probability density $\sum_{x,z} |\psi(x,z)|^2$ of the lowest energy states (MBSs), summed over the cross section of the TI wire, is calculated using the full three-dimensional BHZ model that includes also a superconducting pairing term [see Eq. (F3)]. The MBSs are localized at the ends of the wire. The localization length shrinks as magnetic flux is being increased. For this system, as in the main text in Fig. 4, the critical flux value $\varphi_c \approx 0.065$. The wave functions of the two zero-energy MBSs are antisymmetrized such that they are maximally localized on the left (red) or right (blue). The other parameters are the same as in Fig. 4 of the main text.

FIG. 9. *The lowest and first-excited energies for disordered wires.* We take the average over all lowest state energies ε_0 and the average over all first-excited state energies ε_1 in an ensemble of 30 wires for various strengths of disorder u_0 and flux φ. The full three-dimensional BHZ model includes a superconducting pairing term [see Eq. (F3)] with additional random on-site potential $\Delta\mu(\mathbf{r})$. Even very strong disorder does not substantially move the MBS energy away from zero. For instance, for the largest value of flux in this plot, $\varphi = 0.25$, disorder strengths up to $u_0 \approx 8$ meV do not strongly affect the zero-energy mode and it remains well separated from the SC bulk states. The other parameters are the same as in Fig. 4 of the main text.

square cross section of the TI wire, at two different fluxes are shown in Fig. 8.

APPENDIX G: DISORDER

The appearance of MBSs that are pinned to zero energy for a large region of parameters indicates that MBSs in gated TI wires can be expected to be very stable against various types of disorder, in particular fluctuations of the local chemical potential. This is important because present-day bulk insulating TI wires are relatively dirty, and transport in them is diffusive [16]. Of particular importance are charged impurities in the bulk of thick TI samples which can lead to long-range ≈50 nm fluctuations of the surface chemical potential up to several meV [37–40] (so-called surface puddles). In this context thin wires are better due to the increased screening of these bulk charges by the surface states [41] and the screening of the superconductor itself. As such the magnitude and length of surface puddles in Majorana devices will likely be signifi-

cantly smaller than in bulk TIs that are not in proximity to a superconductor.

Given the complexity of modeling different contributions to disorder in TI wire devices and the screening physics of charged disorder, we leave more realistic modeling for further investigation. Nonetheless, in order to assess the stability of MBSs, we introduce on-site fluctuations in the chemical potential $\Delta\mu(\mathbf{r})$ that are drawn randomly from a uniform distribution $\Delta\mu \in [-u_0/2, u_0/2]$. We take the average over all lowest state energies ε_0 and the average over all energies of the first-excited state, ε_1, in an ensemble of 30 wires with different disorder configurations at various strengths of u_0; the results are shown in Fig. 9 for various fluxes φ. We find that the lowest energy state, corresponding to the MBSs, remains strongly pinned to zero energy and well separated from the SC bulk for large disorder strengths. For instance, the ensemble-averaged lowest energy remains at zero up to $u_0 \approx 8$ meV for $\varphi = 0.25$ ($B \approx 2.5$ T). This stability against disorder is a direct consequence of the large phase space for MBSs in the topological phase diagram of our setup.

[1] A. Y. Kitaev, Phys. Usp. **44**, 131 (2001).

[2] D. A. Ivanov, Phys. Rev. Lett. **86**, 268 (2001).

[3] A. Y. Kitaev, Ann. Phys. (NY) **303**, 2 (2003).

[4] G. Volovik, JETP Lett. **70**, 609 (1999).

[5] N. Read and D. Green, Phys. Rev. B **61**, 10267 (2000).

[6] J. Alicea, Rep. Prog. Phys. **75**, 076501 (2012).

[7] L. Fu and C. L. Kane, Phys. Rev. Lett. **100**, 096407 (2008).

[8] M. Z. Hasan and C. L. Kane, Rev. Mod. Phys. **82**, 3045 (2010).

[9] A. Cook and M. Franz, Phys. Rev. B **84**, 201105(R) (2011).

[10] S. S. Hong, J. J. Cha, D. Kong, and Y. Cui, Nat. Commun. **3**, 757 (2012).

[11] B. Hamdou, J. Gooth, A. Dorn, E. Pippel, and K. Nielsch, Appl. Phys. Lett. **103**, 193107 (2013).

[12] S. Cho, B. Dellabetta, R. Zhong, J. Schneeloch, T. Liu, G. Gu, M. J. Gilbert, and N. Mason, Nat. Commun. **6**, 7634 (2015).

[13] Y. C. Arango, L. Huang, C. Chen, J. Avila, M. C. Asensio, D. Grützmacher, H. Lüth, J. G. Lu, and T. Schäpers, Sci. Rep. **6**, 29493 (2016).

[14] L. A. Jauregui, M. T. Pettes, L. P. Rokhinson, L. Shi, and Y. P. Chen, Nat. Nanotechnol. **11**, 345 (2016).

[15] J. Ziegler, R. Kozlovsky, C. Gorini, M.-H. Liu, S. Weishäupl, H. Maier, R. Fischer, D. A. Kozlov, Z. D. Kvon, N. Mikhailov, S. A. Dvoretsky, K. Richter, and D. Weiss, Phys. Rev. B **97**, 035157 (2018).

[16] F. Münning, O. Breunig, H. F. Legg, S. Roitsch, D. Fan, M. Rößler, A. Rosch, and Y. Ando, Nat. Commun. **12**, 1038 (2021).

[17] O. Breunig and Y. Ando, arXiv:2101.12538.

[18] A. M. Cook, M. M. Vazifeh, and M. Franz, Phys. Rev. B **86**, 155431 (2012).

[19] F. de Juan, R. Ilan, and J. H. Bardarson, Phys. Rev. Lett. **113**, 107003 (2014).

[20] F. de Juan, J. H. Bardarson, and R. Ilan, SciPost Phys. **6**, 60 (2019).

[21] E. Prada, P. San-Jose, M. W. de Moor, A. Geresdi, E. J. Lee, J. Klinovaja, D. Loss, J. Nygård, R. Aguado, and L. P. Kouwenhoven, Nat. Rev. Phys. **2**, 575 (2020).

[22] B. A. Bernevig, T. L. Hughes, and S.-C. Zhang, Science **314**, 1757 (2006).

[23] H. Zhang, C.-X. Liu, X.-L. Qi, X. Dai, Z. Fang, and S.-C. Zhang, Nat. Phys. **5**, 438 (2009).

[24] C.-X. Liu, X.-L. Qi, H. J. Zhang, X. Dai, Z. Fang, and S.-C. Zhang, Phys. Rev. B **82**, 045122 (2010).

[25] F. Schulz, K. Plekhanov, D. Loss, and J. Klinovaja, Phys. Rev. Research **2**, 033215 (2020).

[26] J. Klinovaja, M. J. Schmidt, B. Braunecker, and D. Loss, Phys. Rev. Lett. **106**, 156809 (2011).

[27] B. Braunecker, G. I. Japaridze, J. Klinovaja, and D. Loss, Phys. Rev. B **82**, 045127 (2010).

[28] P. Středa and P. Šeba, Phys. Rev. Lett. **90**, 256601 (2003).

[29] D. Flötotto, Y. Ota, Y. Bai, C. Zhang, K. Okazaki, A. Tsuzuki, T. Hashimoto, J. N. Eckstein, S. Shin, and T.-C. Chiang, Sci. Adv. **4**, eaar7214 (2018).

[30] O. E. Casas, L. Arrachea, W. J. Herrera, and A. L. Yeyati, Phys. Rev. B **99**, 161301(R) (2019).

[31] M. Wimmer, A. R. Akhmerov, M. V. Medvedyeva, J. Tworzydło, and C. W. J. Beenakker, Phys. Rev. Lett. **105**, 046803 (2010).

[32] D. Rainis, L. Trifunovic, J. Klinovaja, and D. Loss, Phys. Rev. B **87**, 024515 (2013).

[33] B. A. Volkov and O. A. Pankratov, Pis'ma Zh. Eksp. Teor. Fiz. **42**, 145 (1985) [JETP Lett. **42**, 178 (1985)].

[34] P. M. Ostrovsky, I. V. Gornyi, and A. D. Mirlin, Phys. Rev. Lett. **105**, 036803 (2010).

[35] Y. Zhang and A. Vishwanath, Phys. Rev. Lett. **105**, 206601 (2010).

[36] J. Klinovaja and D. Loss, Phys. Rev. B **92**, 121410(R) (2015).

[37] B. Skinner, T. Chen, and B. Shklovskii, J. Exp. Theor. Phys. **117**, 579 (2013).

[38] B. Skinner and B. I. Shklovskii, Phys. Rev. B **87**, 075454 (2013).

[39] N. Borgwardt, J. Lux, I. Vergara, Z. Wang, A. A. Taskin, K. Segawa, P. H. M. van Loosdrecht, Y. Ando, A. Rosch, and M. Grüninger, Phys. Rev. B **93**, 245149 (2016).

[40] T. Knispel, W. Jolie, N. Borgwardt, J. Lux, Z. Wang, Y. Ando, A. Rosch, T. Michely, and M. Grüninger, Phys. Rev. B **96**, 195135 (2017).

[41] T. Bömerich, J. Lux, Q. T. Feng, and A. Rosch, Phys. Rev. B **96**, 075204 (2017).